P20

The Impact of Hodograph Shape on Hail Production in Idealized Supercell Storms

Eli J. Dennis and Matthew R. Kumjian

Department of Meteorology, The Pennsylvania State University, University, PA

1. INTRODUCTION

Previous research has shown that storm-relative airflow could be as important as updraft speed for hail growth. This research suggests that hail growth is not only a function of the dynamics of the supercell structure, but also of the number concentration of hail growth embryos, and of the cloud mixing ratio. Previous research has shown that hail growth can occur from numerous initial conditions, but the favorable initial region for the smaller and more numerous embryos that are meant to dominate is restricted (Foote 1984). The width of the updraft is also found to be an important factor in limiting hail growth (Foote 1984). The purpose of this study is to determine how the hodograph structure of supercell thunderstorm environments affects the diameter of hailstones and the area impacted by a hail event.

2. FACTORS THAT AFFECT HAIL GROWTH

2.1 Supercell Dynamics

Supercell dynamics in large part are governed by the vertical distribution of storm-relative horizontal winds. Such factors are used to differentiate the types of supercells, and provide a basis for the reasons events occur or do not occur. For hail formation, very specific dynamical structures need to be present in the storm-relative flow field. Previous studies have suggested a critical factor is a broad region of moderate updraft allowing hailstones to remain balanced in the primary region where efficient growth occurs (e.g., Nelson 1983). The primary growth region lies between 4.5–8 km above the surface when considering the Weisman and Klemp (1982) sounding. For large hail growth, the storm structure must be such that the hailstones experience prolonged exposure to the moisture rich updraft region (Miller et al. 1988). This region contains the appropriate temperature and moisture available for hail growth.

Corresponding author address: Dr. Matthew Kumjian, The Pennsylvania State University, 513 Walker Building, University Park, PA 16802; email: kumjian @psu.edu

This dynamical structure of a supercell, including the mesocyclone, is of paramount importance in whether or not a significant hail event occurs.

2.2 Number Concentration

Hail growth is a direct product of the number concentration of hailstone embryos. The available hailstone embryo must compete for a limited amount of cloud water available within the optimum hail growth region (Browning and Foote 1976). The embryos, according to supercell simulations, are most commonly entrained from the south side of the bounded weak echo region. They can originate in the forward flank region, and get wrapped into the updraft following the horizontal flow field.

2.3 Cloud Mixing Ratio

The cloud mixing ratio quantifies the amount of liquid in the form of cloud droplets available to be collected by embryos for hail growth to occur. When many particles are available for hail growth, the environment becomes very competitive. The embryonic particles compete over the amount of available water mass.

3. MODEL SPECIFICS

The numerical model used for this study was Cloud Model 1 version 17 (CM1v17; e.g., Bryan and Fritsch 2002). The domain was a 240 x 240 x 80 grid with 500-m grid spacing in the x- and y- dimensions and a vertical grid spacing of 250 m. The microphysics scheme used was the Morrison 2-moment scheme, which predicts both the hail mass mixing ratio and number concentration mixing ratio (Morrison et al. 2009). This physics parameterization scheme was chosen because the two moments were desired to create new metrics used to evaluate differences in hail swaths. We ignored surface and radiative fluxes. The top and bottom of the modeled domain is rigid, with a Rayleigh dampening layer in effect in the upper 5 km. The lateral boundaries are open. The domain is adjusted to move with the simulated storm.

4. EXPERIMENTAL METHODS

All simulations were based on the standard idealized supercell case using the Weisman and Klemp (1982) sounding. Each hodograph is based on Weisman and Rotunno (2000), but its structure was adjusted to produce 20 different simulated supercell storms (Fig. 1). The storms that this study focused on were Control (Test Supercell Case), 2.0cos(u), 2.0sin(v), 2.0cos(u)2.0sin(v), umax41, and vmax16.

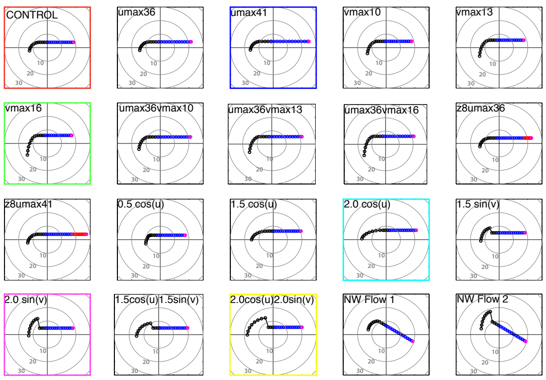

Figure 1: Hodograph structures for each of the simulated supercell storms, as well as the naming convention for each storm. The highlighted storms were the focus of the study, including: CONTROL (Test Supercell Case), umax41, vmax16, 2.0cos(u), 2.0sin(v) and 2.0cos(u)2.0sin(v).

The differences in the hodograph shapes altered the dynamic structures of the simulated supercell. But, to ensure that changes in hail production are primarily attributable to differences in hodograph shape, we must ensure that the hodograph changes did not significantly alter the magnitude of the updraft velocity. As seen in Figure 2, maximum updraft speeds were not substantially different among the different simulations.

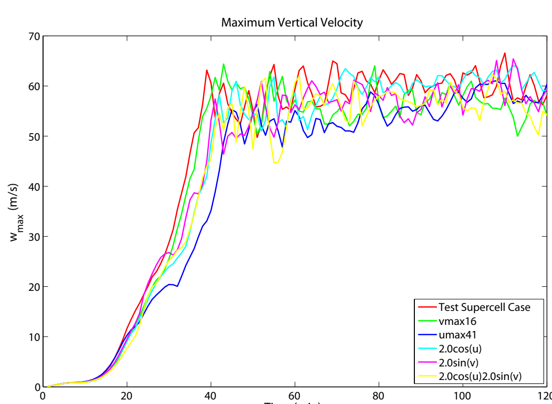

Figure 2: Maximum updraft magnitude in each of the highlighted supercell storms. It is apparent that the maximum updraft in each storm is not significantly different.

5. RESULTS

5.1 Dynamic influence on hail growth

Ideally, to optimize hail growth, there needs to be ample liquid water available, with a limited number concentration of embryos. Each of those embryos needs to be entrained through a wide shoulder region of the updraft. The updraft magnitude cannot be too strong compared to the fall speed of the growing particles, or else the particles will be ejected out the top of the primary growth region (where liquid water does not exist in sufficiently large amounts) before they can achieve significant mass. The longer these particles can stay balanced within the optimal growth region, the more growth will occur. The optimum structure for hail growth includes a specific orientation of the updraft's major horizontal axis, a shallow gradient in the magnitude of updraft velocity near the particle injection region, and horizontal wind structure that favors injection of particles from the southern side of the bounded weak echo region driven by the rear flank gust front.

First, consider the orientation of the updraft's major axis. Figure 3 shows cross-sections of simulated supercell thunderstorms at 7.125 km AGL. The six cases each have an updraft contoured in yellow, (the values are discussed in the caption). Focus on the shape of the updraft contours in the top central frame, umax41, and in the bottom central frame, 2.0sin(v). These correspond to the cases with the largest westerly and southerly shear, respectively. The differing shear values have distorted the updraft shape to favor the strongest wind vector. In umax41, the updraft has been elongated in the east-west direction, while the 2.0sin(v) updraft contours have been elongated in the north-south direction. The orientation of the updraft has the effect of limiting the inflow regions of particles that serve as growth embryos. The particles entering the updraft are entrained through the bottom of the BWER. The area of entrainment of particles in storms with strong westerly shear is more efficient due to the wider injection region.

Secondly, the gradient of updraft strength is important for hail growth processes to occur. In observing the top central storm in Fig. 3 (umax41), notice that there is a region upstream of the RFGF where the gradient of the updraft is very weak compared to that of the storms oriented in the north-south direction. Also, note that to the west of the BWER, but still within the updraft, there is a similar region of weak updraft gradient that is not apparent in the strong northerly storms. This area of the updraft is imperative for hail growth. Particles enter the updraft and get propelled upward. If the magnitude of

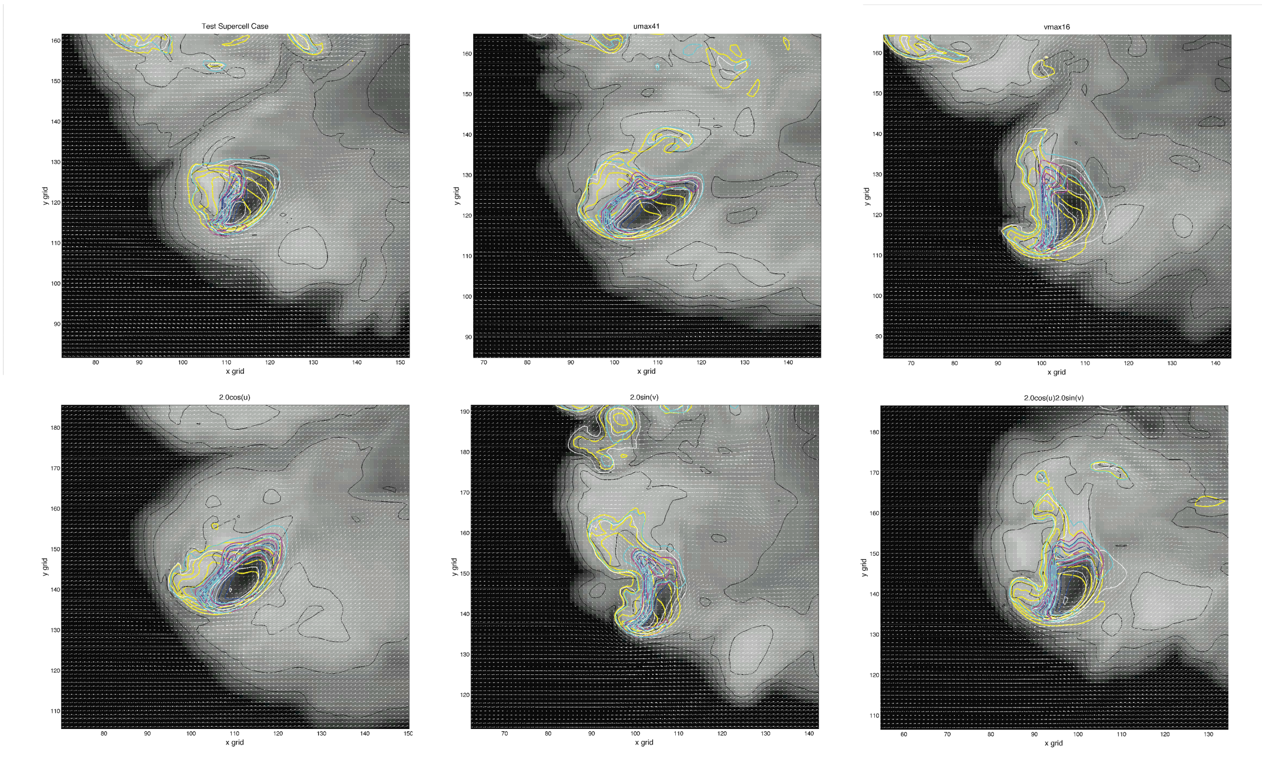

Fig 3: Shows horizontal slices through each of the highlighted storms, 1 hour and 30 minutes into the simulations. The horizontal surface is located at 7.125 km above the surface. The figure includes several contoured values. Yellow contour lines depict updraft, at 10, 20, 30, and 40 m s^{-1}. Dark blue contour lines show rain bands with contour values of 0.0001, 0.0025, 0.005, 0.0075, and 0.01 [kg kg^{-1}]. Magenta, cyan, and green contour lines indicate hail growth processes, (freeze conversion, rime growth, and rime conversion, respectively). Freeze conversion and rime growth have contour values of $0.1e^{-4}$, $0.5e^{-4}$, $1e^{-4}$, $1.5e^{-4}$, and $2.0e^{-4}$ (kg kg^{-1} s^{-1}). The rime conversion contour values are $0.1e^{-5}$, $0.5e^{-5}$, $1.0e^{-5}$, $1.5e^{-5}$, and $2.0e^{-5}$ (kg kg^{-1} s^{-1}). The thin black contours indicate reflectivity at 30, 40 and 50 dBz. The white contour lines show clouds determined by cloud mixing ratio, q_G, with contour values of 0.0001, 0.0025, 0.005, 0.0075, and 0.01 [kg kg^{-1}]. The greyscale color ramp shows reflectivity at that height [dBz]. The white arrows are wind vectors that show the horizontal wind field [m s^{-1}].

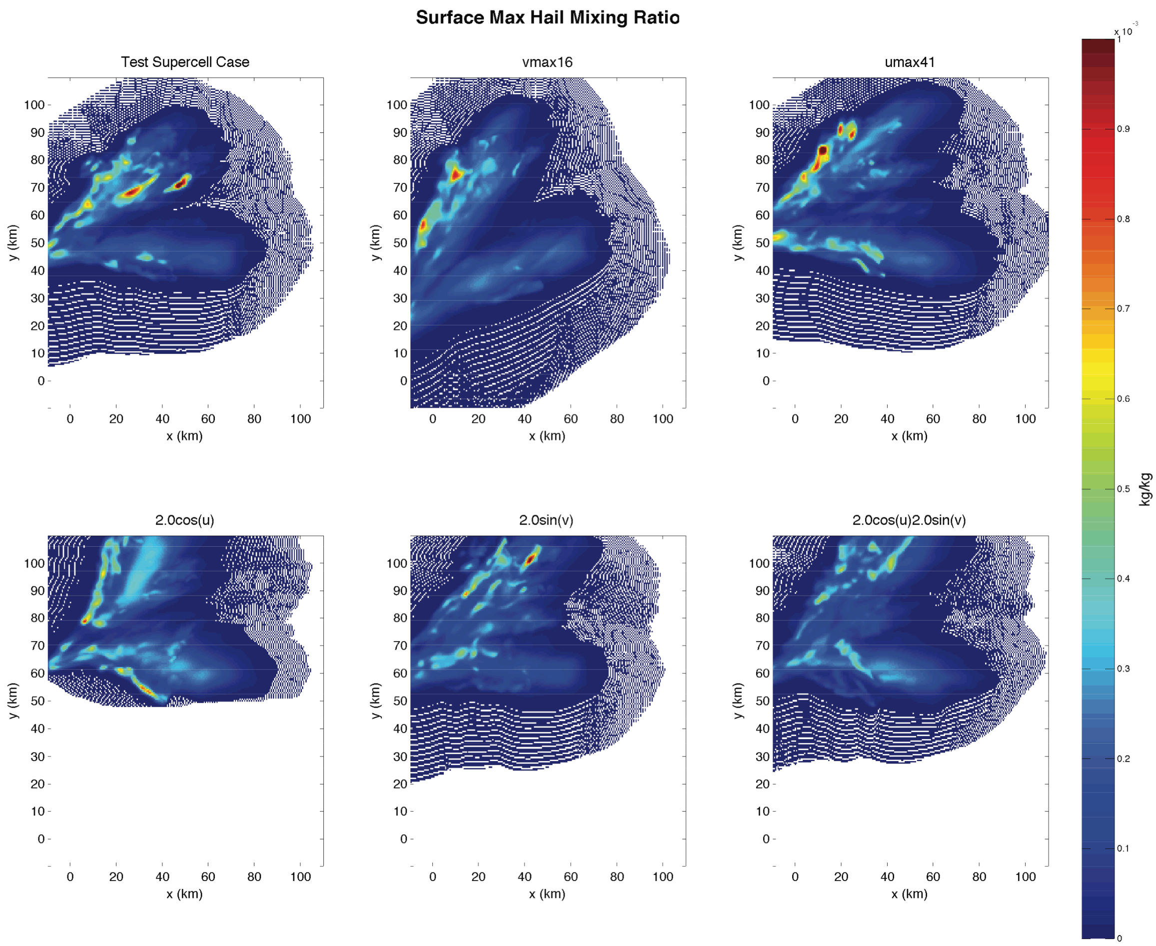

Fig 4: Time-integrated maximum hail mass mixing ratio at the surface with a moving domain. These swaths show the maximum mixing ratio of hailstones in kg kg^{-1} at each grid point at the surface throughout the 2-hour storm duration for each of the highlighted supercell storms.

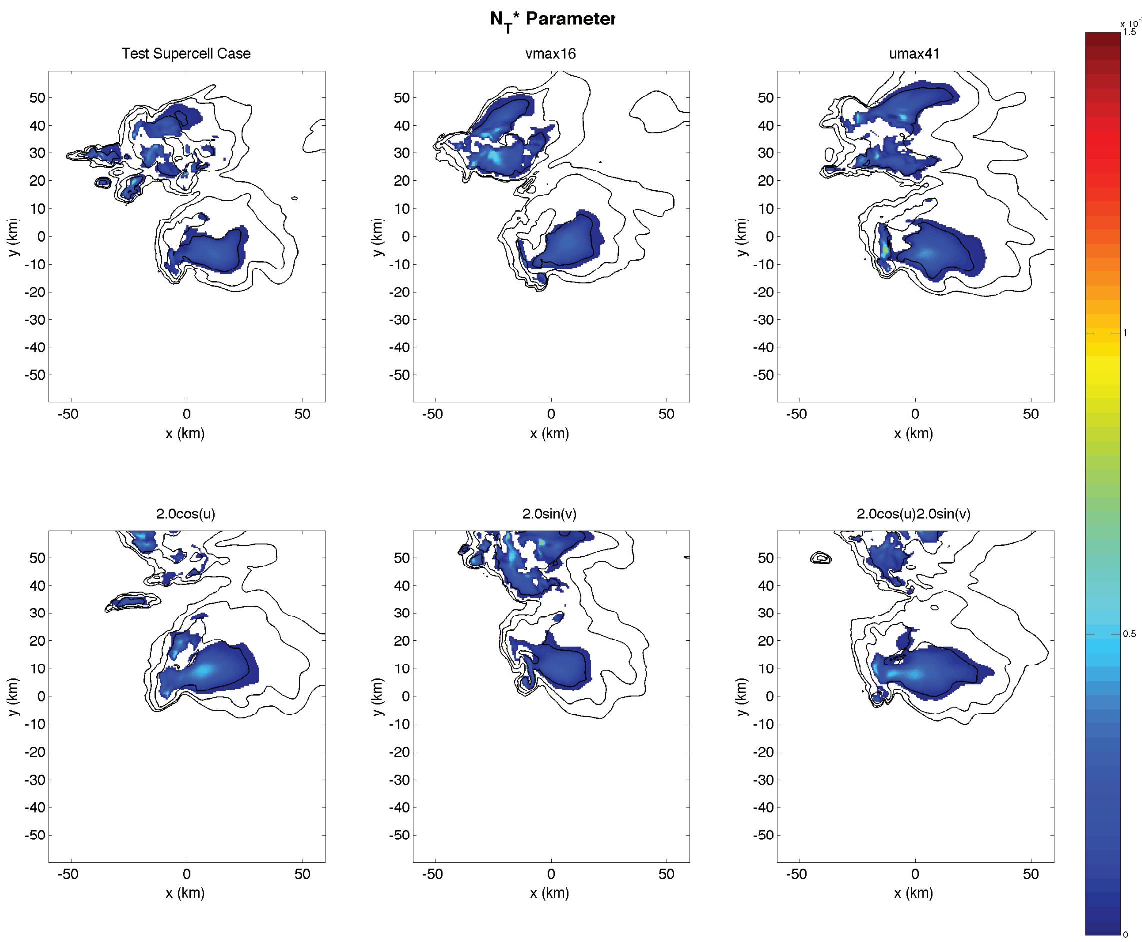

Fig 5: The color scale shows the developed hail metric, N_T^*. It quantifies the hailstones exceeded the "severe" threshold. The contour lines indicate radar reflectivity in dBz from 30 dBz to 50 dBz in 10-dBz increments. The hail metric has units of [m^{-3}].

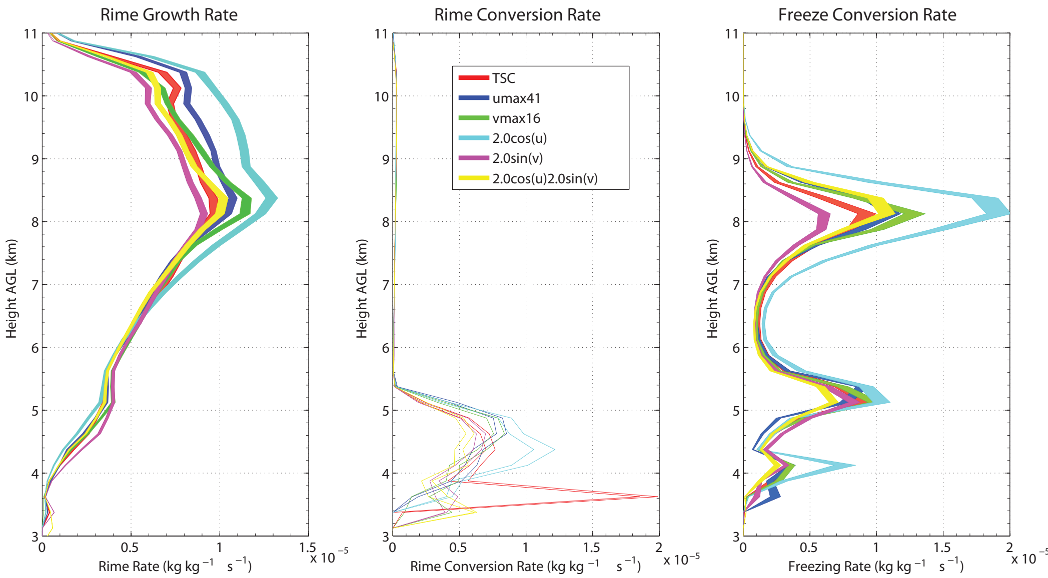

Fig. 6: Compares the hail growth processes of each storm. 95% confidence intervals around the mean process rate at each height level are shaded. The confidence intervals were calculated using a bias-corrected-and-accelerated bootstrapping technique (e.g., Efron and Tibshirani 1993). Non-overlapping confidence intervals are interpreted as statistically significant differences in the means between the different simulations at the 95% confidence level.

the gradient of the updraft is too large, the particles enter strong updraft regions too quickly and are ejected out of the top of the optimal growth region. For maximum hail mass to be achieved, particles must remain balanced in the optimal growth region for the longest period of time. That does not necessarily mean the strongest updraft region, but the correct updraft region for the growing particles' fall speeds.

Thirdly, the storm dynamics must be typical of most right-moving supercell thunderstorms, in that, the RFGF wraps cyclonically around the western edge of the hook echo. This wrapping brings particles generated aloft through the western portion of the mesocyclone and around the BWER towards the region where particle injection occurs on the south side of the BWER. This particle injection is pivotal for hail formation. This horizontal flow pattern is evident in each storm simulation in the horizontal wind vectors (see Fig. 3).

5.2 Developed quantification metrics

Previously, the quantification of hail at the surface in CM1 was the time-integrated maximum hail mass mixing ratio. This output field leaves the quantification vulnerable to ambiguity because it does not account for the second predicted variable (number mixing ratio). The value of the time-integrated maximum hail mass mixing ratio could be equal if, for example, many 1-cm sized hailstones fell, or if just a few softball-sized hailstones fell. This is an exaggerated example, but it conveys the point. There were two metrics developed to quantify the amount of hail: a proxy for hail kinetic energy, **K**, and a parameter to evaluate the number concentration of hailstones in excess of a certain diameter threshold, N_T^*.

5.2.1 Kinetic Energy Parameter, K

In an effort to combine the information about the kinetic energy of the simulated hail (i.e., make use of the information about both predicted model parameters), a normalized hail kinetic energy parameter **K** was developed. To do so, the mass- and number concentration weighted fall speeds ($\mathbf{V}_q$ and $\mathbf{V}_N$, respectively) are multiplied:

$$\mathbf{V}_q = \frac{\int_0^\infty N(D)m(D)v_h(D)dD}{\int_0^\infty N(D)m(D)dD} \tag{1}$$

$$\mathbf{V}_N = \frac{\int_0^\infty N(D)v_h(D)dD}{\int_0^\infty N(D)dD} \tag{2}$$

where

$$v_h(D) = \alpha_h D^{\beta_h} \tag{3}$$

is the parameterized fall speed of hailstones, and

$$m(D) = \frac{\pi}{6}\rho_h D^3 \tag{4}$$

is the mass of the hailstones (assuming spherical geometry). In the velocity relation (3), the parameters used in Morrison's two-moment scheme are

$$\alpha_h = 114.5 \text{ m}^{0.5} \text{ s}^{-1}$$
$$\beta_h = 0.5$$

Solving equations (1) and (2) and multiplying the results leads to the kinetic energy parameter, ($\text{m}^2 \text{ s}^{-2}$ or J kg^{-1}).

$$\mathbf{K} \equiv \mathbf{V}_N\mathbf{V}_q = \frac{[\alpha_h\Gamma(1+\beta_h)]^2}{6\Lambda^{2\beta_h}} \tag{5}$$

In eqn. (5), Γ is the complete gamma function. The two predicted variables q_h and N_{Th} that come directly from the model output are used to compute hail size distribution slope parameter Λ. **K** is helpful to quantify the amount of kinetic energy apparent in a hail event that affects the surface.

*5.2.2 Number Concentration Parameter, N_T**

The number concentration parameter N_T^* quantifies the amount of hail exceeding a certain size that reaches the surface. The N_T^* parameter mitigates this ambiguity presented in the time-integrated maximum hail mass mixing ratio quantity by incorporating both of the prognostic variables from the Morrison two-moment microphysics scheme to create a value for hailstones occurring that are larger than the defined "severe" diameter threshold, which is herein set to 2.54 cm. N_T^* is defined as

$$N_T^* \equiv N_{Th}(D > D_{SVR}) = \int_{D_{SVR}}^\infty N(D)dD \tag{6}$$

An upper-tailed incomplete gamma function is required because we are not integrating over the entire spectrum of sizes:

$$\gamma^+(x, a_{SVR}) = \int_{a_{SVR}}^\infty \exp(-a)a^{x-1}da \tag{7}$$

where a is substituted (via change of varibles) $a = \Lambda D$ in eqn. (7). Doing so, and combing eqns. (6) and (7) results in

$$N_T^* = \frac{N_o}{\Lambda}\gamma^+(1, D_{SVR}) \tag{8}$$

To come up with a threshold for N_T^*, the effects of large hailstones on a common-sized surface was considered. Doing so requires knowledge of the fall speeds hailstones. An area comparable to a roof of a single family home, roughly A = 100 m^2, was considered. The number of hailstones hitting such an area depends on the flux of hail, $\mathbf{F}_h$:

$$\mathbf{F}_h = N_T^* \times v_h(D_{SVR}) \tag{9}$$

where the velocity of falling hail, v_h, is a function of the diameter of the hailstones (eqn. 3). This flux can be integrated over a given amount of time, such as a radar volume scan (Δt ~ 300 s). Thus the minimum threshold for N_T^*can be written:

$$N^*_{T_{thresh}} = \frac{1}{v_h(D_{SVR}) \cdot A \cdot \Delta t} \tag{10}$$

Now compare the N_T^* parameter and the time-integrated maximum hail mass mixing ratio in Figs. 5 and 6. In both of the 6-panel plots, focus on the top right panel, and compare it to the bottom center panel. These panels are storms: umax41 (largest westerly shear), and 2.0sin(v) (largest southerly shear), respectively. The values in the teal blue color in Fig. 4, are approximately $\approx$0.4 kg kg^{-1} for both of the storms, which could be misleading. The storms produced significantly different amounts of hail in excess of the defined threshold (2.54 cm or 1 in). Now, notice the same panels with the new metric in Fig. 5. The high values of N_T^* are co-located with the location of the typical growth region of hail in the right-moving supercell. The enhanced N_T^* values in the umax41 storm suggest that more hail was produced in excess of 2.54 cm in diameter than was produced by the 2.0sin(v) storm simulation. This conclusion could not have been drawn from the time-integrated maximum hail mass mixing ratio field.

5.3 Analysis of process rates

To determine how changes in storm flow structure affected hail growth in the simulations, we analyzed important microphysical process rates that contribute to hail formation and growth. The individual microphysical processes have been grouped into three main categories: rime conversion, which represents the conversion of particles to the hail category upon sufficiently large amounts of riming; rime growth, which is mass added to the hail category by subsequent riming by liquid water; and freeze conversion, in which liquid droplets freeze and are transferred to the hail category. Domain-averaged vertical profiles of these process-rates are shown in Figure 6. The 95% confidence interval about the average vertical profiles is computed using the bias-corrected-and-accelerated bootstrapping technique (e.g., Efron and Tibshirani 1993). When the confidence intervals do not overlap, the differences can be considered statistically significant at the 95% confidence level.

Clear statistically significant differences between the different simulations are evident, particularly aloft. The 2.0cos(u) and umax41 simulations have the largest rime growth rates, whereas 2.0sin(v) has the smallest. Thus, a contributor to the larger hail production in the west-east-oriented updraft cases is enhanced rime growth aloft. Freeze conversion is also much larger for the 2.0cos(u) case, with 2.0sin(v) having the smallest freezing conversion aloft. This implies less liquid water mass being lofted to such heights in the 2.0sin(v) case. Rime conversion rates differences are not as noticeable, though 2.0cos(u) does reveal a statistically significantly larger maxima in the 4 – 5 km AGL layer, implying more mass is converted to hail via heavy riming in this layer than in the other cases.

6. CONCLUSIONS

In summary, the hodograph shape can alter the hail swaths at the surface even given the same thermodynamic structure. The differences in hail production are explained by different dynamic structures that have a large effect on the number concentration of hailstones in primary growth regions of supercell storms. The storms with more west-east oriented updrafts (e.g., umax41) seemingly have better geometry for hail growth, leading to more hail production than the more north-south oriented updrafts (e.g., 2.0sin(v)). These differences arise because the west-east-oriented updrafts have wider regions for embryo injection and more optimal gradients in vertical velocity to suspend growing particles. Two new metrics were developed to quantify the amount of hail that impacts the surface and to assess hail damage in NWP models, taking a preliminary step towards future NWP-based assessments of hail risk.

ACKNOWLEDGEMENTS

The authors would like to thank the Insurance Institute for Business and Home Safety (IBHS) for providing funding for this study. Drs. Tanya Brown and Ian Giammanco (IBHS) are thanked for their support and insights. We are grateful to Dr. George Bryan and Dr. Hugh Morrison (NCAR) and Dr. Zachary Lebo (CIRES/Univ. of Colorado) for helping with the CM1 code.

REFERENCES

Browning, K. A. and Foote, G. B. (1976), Airflow and hail growth in supercell storms and some implications for hail suppression. Q.J.R. Meteorol. Soc., 102: 499–533. doi: 10.1002/qj.49710243303

Bryan, G. H. and M. J. Fritsch, 2002: A benchmark simulation for moist nonhydrostatic numerical models. *Mon. Wea. Rev.*, **130**, 2917-2928.

Efron, B., and R. J. Tibshirani, 1993: *An Introduction to the Bootstrap.* Chapman and Hall, 456 pp.

Foote, G. B., 1984: A study of hail growth utilizing observed storm conditions. *J. Climate Appl. Meteor.*, **23**, 84–101.

Morrison, H., G. Thompson, and V. Tatarskii, 2009: Impact of cloud microphysics on the development of trailing stratiform precipitation in a simulated squall line: Comparison of one- and two-moment schemes. *Mon. Wea. Rev.*, **137**, 991–1007.

Miller, L. J., J. D. Tuttle, and C. A. Knight, 1988: Airflow and hail growth in a severe Northern High Plains supercell. *J. Atmos. Sci.*, **45**, 736–762.

Nelson, S. P., 1983: The influence of storm flow structure on hail growth. *J. Atmos. Sci.*, **40**, 1965–1983.

Weisman, M. L., and J. B. Klemp, 1982: The dependence of numerically simulated convective storms on vertical wind shear and buoyancy. Mon. Wea. Rev.,110, 504–520.

——, and ——, 1984: The structure and classification of numerically simulated convective storms in directionally varying wind shears. *Mon. Wea. Rev*.,**112**, 2479–2498.

——, and ——, 1986: Characteristics of isolated convective storms. *Mesoscale Meteorology and Forecasting*, P. S. Ray, Ed., Amer. Meteor. Soc., 331–358.

——, and R. Rotunno, 2000: The use of vertical wind shear versus helicity in interpreting supercell dynamics. *J. Atmos. Sci.*, **57**, 1452-1472.